# Thick-shelled, grazer-protected diatoms decouple ocean carbon and silicon cycles in the iron-limited Antarctic Circumpolar Current

Philipp Assmy[a,b,1], Victor Smetacek[b,c,1], Marina Montresor[d], Christine Klaas[b], Joachim Henjes[b], Volker H. Strass[b], Jesús M. Arrieta[e,f], Ulrich Bathmann[b,g], Gry M. Berg[h], Eike Breitbarth[i], Boris Cisewski[b,j], Lars Friedrichs[b], Nike Fuchs[b], Gerhard J. Herndl[e,k], Sandra Jansen[b], Sören Krägefsky[b], Mikel Latasa[l,m], Ilka Peeken[b,n], Rüdiger Röttgers[o], Renate Scharek[l,m], Susanne E. Schüller[p], Sebastian Steigenberger[b,q], Adrian Webb[r], and Dieter Wolf-Gladrow[b]

[a]Norwegian Polar Institute, 9296 Tromsø, Norway; [b]Alfred Wegener Institute Helmholtz Centre for Polar and Marine Research, 27570 Bremerhaven, Germany; [c]National Institute of Oceanography, Dona Paula, Goa 403 004, India; [d]Stazione Zoologica Anton Dohrn, 80121 Napoli, Italy; [e]Department of Biological Oceanography, Royal Netherlands Institute for Sea Research, 1790AB, Den Burg, Texel, The Netherlands; [f]Department of Global Change Research, Instituto Mediterraneo de Estudios Avanzados, Consejo Superior de Investigaciones Científicas–Universidad de las Islas Baleares, 07190 Esporles, Mallorca, Spain; [g]Leibniz Institute for Baltic Sea Research Warnemünde, 18119 Rostock, Germany; [h]Department of Geophysics, Stanford University, Stanford, CA 94305; [i]Helmholtz Institute for Ocean Research Kiel, 24105 Kiel, Germany; [j]Thünen Institute of Sea Fisheries, 22767 Hamburg, Germany; [k]Department of Marine Biology, Faculty Center of Ecology, University of Vienna, 1090 Vienna, Austria; [l]Centro Oceanográfico de Gijón/Xixón, Instituto Español de Oceanografía, E-33212 Gijón/Xixón, Asturias, Spain; [m]Institut de Ciències del Mar, Consejo Superior de Investigaciones Científicas, 08003 Barcelona, Spain; [n]MARUM–Center for Marine Environmental Sciences, University of Bremen, 28359 Bremen, Germany; [o]Institute for Coastal Research, Helmholtz-Zentrum Geesthacht, Centre for Materials and Coastal Research, 21502 Geesthacht, Germany; [p]Department of Marine Science, University of Otago, Dunedin 9054, New Zealand; [q]National Oceanography Centre, University of Southampton Waterfront Campus, Southampton SO14 3ZH, United Kingdom; and [r]Department of Oceanography, University of Cape Town, Rondebosch 7701, South Africa

Diatoms of the iron-replete continental margins and North Atlantic are key exporters of organic carbon. In contrast, diatoms of the iron-limited Antarctic Circumpolar Current sequester silicon, but comparatively little carbon, in the underlying deep ocean and sediments. Because the Southern Ocean is the major hub of oceanic nutrient distribution, selective silicon sequestration there limits diatom blooms elsewhere and consequently the biotic carbon sequestration potential of the entire ocean. We investigated this paradox in an in situ iron fertilization experiment by comparing accumulation and sinking of diatom populations inside and outside the iron-fertilized patch over 5 wk. A bloom comprising various thin- and thick-shelled diatom species developed inside the patch despite the presence of large grazer populations. After the third week, most of the thinner-shelled diatom species underwent mass mortality, formed large, mucous aggregates, and sank out en masse (carbon sinkers). In contrast, thicker-shelled species, in particular *Fragilariopsis kerguelensis*, persisted in the surface layers, sank mainly empty shells continuously, and reduced silicate concentrations to similar levels both inside and outside the patch (silica sinkers). These patterns imply that thick-shelled, hence grazer-protected, diatom species evolved in response to heavy copepod grazing pressure in the presence of an abundant silicate supply. The ecology of these silica-sinking species decouples silicon and carbon cycles in the iron-limited Southern Ocean, whereas carbon-sinking species, when stimulated by iron fertilization, export more carbon per silicon. Our results suggest that large-scale iron fertilization of the silicate-rich Southern Ocean will not change silicon sequestration but will add carbon to the sinking silica flux.

evolutionary arms race | top-down control | geo-engineering

Diatoms—silica-shelled unicellular phytoplankton—are major exporters of organic carbon from the surface to the deep ocean and sediments and, hence, influence ocean nutrient cycles and atmospheric $CO_2$ levels (1, 2). However, silicate concentrations, for which diatoms have an obligate demand, vary widely over the nutrient-rich regions of the oceans (3). This is largely due to processes decoupling silicon cycling from that of other nutrients and carbon in surface waters of the Antarctic Zone (AZ), the southernmost belt of the Antarctic Circumpolar Current (ACC) (4). Thus, Si concentrations decline across the AZ

from >70 mmol $Si \cdot m^{-3}$ in upwelling waters along its southern boundary (the Antarctic Divergence) (5) to <5 mmol $Si \cdot m^{-3}$ along the Antarctic Polar Front (APF) (6). The corresponding decline in nitrate is much smaller, from 30 to 23 mmol $N \cdot m^{-3}$. The resulting Si/N export ratio of 9/1 is much higher than the average diatom Si/N ratio of ~1/1 (7, 8). The paradox (9) can partly be explained by increasing Si/N ratios with iron deficiency recorded in many species (10–13) in addition to the exceptionally thick frustules of some ACC diatom species (14), which can reach Si/N ratios of >4:1 in *Fragilariopsis kerguelensis* (15).

A portion of the silica shells (frustules) sinking out of the northward-propagating surface Ekman layer dissolves in the southward-propagating deep water and is returned as Si to the surface in

## Significance

Silica-shelled diatoms dominate marine phytoplankton blooms and play a key role in ocean ecology and the global carbon cycle. We show how differences in ecological traits of dominant Southern Ocean diatom species, observed during the in situ European Iron Fertilization Experiment (EIFEX), can influence ocean carbon and silicon cycles. We argue that the ecology of thick-shelled diatom species, selected for by heavy copepod grazing, sequesters silicon relative to other nutrients in the deep Southern Ocean and underlying sediments to the detriment of diatom growth elsewhere. This evolutionary arms race provides a framework to link ecology with biogeochemistry of the ocean.

upwelling water along the Antarctic Divergence (1). This vertical recycling loop between surface and deep water supports growth of thick-shelled diatoms in the surface and functions as a global ocean silicon trap in the deep-water column. Another portion, mainly comprising robust frustules of comparatively few species, of which *Fragilariopsis kerguelensis* and *Thalassiothrix antarctica* are particularly common (16–18), is buried as diatom ooze in sediments underlying the iron-limited ACC, which functions as a major global silicon sink (19), accounting for 42–48% of the total marine silica removal (20). In contrast, the sediments underlying productive regions in the ACC, where phytoplankton blooms fertilized by iron input from land masses (21, 22), shelf sediments or dust occur regularly (23), have 10-fold higher carbon contents (>2% C of dry matter) (24), and are dominated by spores of the ubiquitous diatom genus *Chaetoceros* (25, 26).

The massive removal of silicon relative to nitrogen from the surface layer by the diatoms of the low-productive, iron-limited AZ ecosystem implies that, in addition to the heavy silicification of ACC diatoms (14), a significant proportion of their nitrogen demand will have to be provided by a highly efficient recycling system in the surface layer (27). In contrast to phytoplankton, copepod-dominated zooplankton stocks of high-nutrient, low-chlorophyll (HNLC) regions of the oceans are comparatively large (28, 29). In fact, their grazing pressure was considered to control phytoplankton biomass in HNLC regions before iron limitation was firmly established (30). It has since been hypothesized that copepod feeding and defecation are part of the recycling system (31) and that the phytoplankton species that accumulate biomass in the face of heavy grazing pressure will have evolved some form of defense (32), most likely the heavily silicified frustules characteristic of ACC diatoms (14).

As the Si-depleted northern ACC surface layer is the major source of nutrients upwelling in low latitudes (4), Si retention in the ACC constrains diatoms from forming blooms over large, nutrient-rich areas of the ocean (3) with far-reaching repercussions on food webs and ocean carbon sequestration. A better understanding of the deep water silicon trap and sedimentary sink is necessary to explain functioning of the glacial Southern Ocean (33) and its impact on $CO_2$ drawdown, but also to predict the response of Southern Ocean biota to large-scale and long-term artificial iron fertilization (34). Ocean iron fertilization experiments provide the necessary conditions for the quantitative investigation of these mechanisms because they simulate the effect of natural iron input on pelagic ecosystems with their full complement of grazers and pathogens (34).

## Results and Discussion

**The Experiment.** The European Iron Fertilization Experiment (EIFEX) was carried out during RV *Polarstern* cruise ANT-XXI/3 in late austral summer [11 February (day −1) to 20 March (day 36) 2004] in the 60-km diameter, clockwise rotating core of a mesoscale, vertically coherent eddy extending to the seafloor at ~3,700-m depth and enclosed in a meander of the APF centered at 49°S, 2°E in the Atlantic sector of the Southern Ocean (35). The circular patch of initially 167 $km^2$ had spread to 798 $km^2$ by day 19 and completed four rotations within the eddy by day 36. In-stations were placed in the least diluted region (the hot spot) of the patch, hence sampled the same water mass throughout. Out-stations were always located within the closed core of the eddy, well away from the patch (35). Vertical coherence of the deep-water column with the overlying surface layer was confirmed by the trajectories of four autonomous APEX floats positioned between 200- and 1,000-m depth, as well as two independent models based on hydrographical profiles to the seafloor and on satellite altimetry (35).

Here, we show that the strong biogeochemical response to iron addition (35) was closely linked to temporal changes in the populations of dominant diatom species in surface, subsurface,

and deeper layers. Standing stocks (carbon per square meter) are derived from trapezoidal integration of measurements carried out on six to nine discrete water samples taken from standard depths at 10- to 20-m intervals in the 100-m mixed layer (35), 50-m intervals in the 200- to 350-m depth layer, and larger intervals for the deep-water column down to the seafloor. In addition to full (living) cells, intact empty and broken diatom frustules, empty and damaged tintinnid loricae and copepod fecal pellets were counted under a light microscope to assess species-specific diatom and tintinnid mortality and grazing by the copepod assemblage. Empty frustules and loricae can be caused by (*i*) cell death, (*ii*) sexual reproduction, (*iii*) viral infection, or (*iv*) protozoan and metazoan grazing, whereas broken frustules and damaged loricae are due to handling by copepod mandibles (36). Stocks of particulate organic carbon (POC) and nitrogen (PON), chlorophyll *a* (Chl *a*), and biogenic silica (BSi) were highly correlated ($P << 0.05$) with total plankton, phytoplankton, and diatom carbon (DC), respectively, as estimated from organism counts (Figs. 1 and 2*B*).

**Plankton Trends.** *The initial situation.* During the initial mapping of the eddy, nitrate, phosphate, and silicate concentrations inside
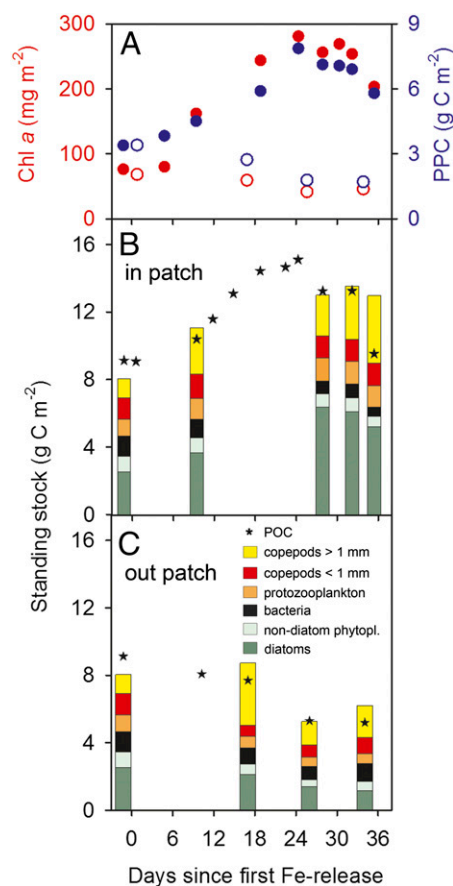


**Fig. 1.** Chl *a*, phytoplankton carbon (PPC), and integrated stocks of plankton composition in the 100-m surface layer inside and outside the fertilized patch. (*A*) PPC calculated from biovolume data (blue circles) and Chl *a* stocks (red circles). The full and open circles are for inside and outside the fertilized patch, respectively. Total plankton carbon (bars) and particulate organic carbon (POC) (stars) stocks inside (*B*) and outside (*C*) the patch with the contributions of diatoms, nondiatom phytoplankton (largely nanoflagellates: solitary *Phaeocystis* cells and *Prorocentrum* spp.), bacteria, protozooplankton (largely heterotrophic dinoflagellates, ciliates, and acantharia), small copepods <1 mm (including nauplii, small copepodites, and *Oithona*), and large copepodites and adult copepods >1 mm.
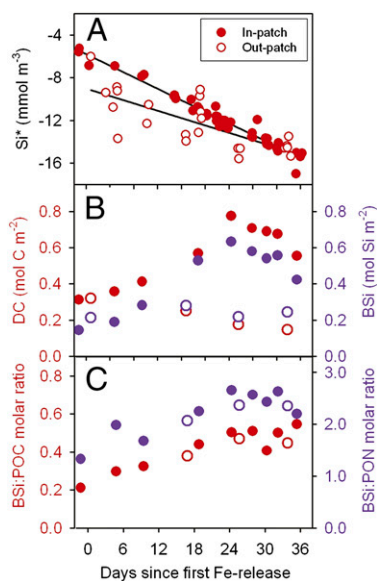
**Fig. 2.** Silicon dynamics in relation to carbon and nitrogen. (*A*) Uptake of Si inside (full circles) and outside (open circles) the patch expressed as Si* (Si–nitrate concentrations). Because nitrate decreased only slightly, Si* values parallel Si concentrations. The greater scatter in out-patch values is explained by spatial heterogeneity in the core outside the patch (in-patch: $r^2 = 0.96$, $P < 0.0001$; out-patch: $r^2 = 0.58$, $P < 0.0001$). (*B*) Biogenic silica (BSi) (blue) and diatom carbon stocks including equivalent carbon content of empty and broken frustules (DC) (red) for direct comparison with BSi. (*C*) Ratios of biogenic silica to particulate organic carbon (BSi/POC) (red), and of biogenic silica to particulate organic nitrogen (BSi/PON) (blue). Note similarity in ratios outside and inside the patch.

the core were 24.5–25 mmol N·m$^{-3}$, 1.7–1.8 mmol P·m$^{-3}$, and 14–19 mmol Si·m$^{-3}$, respectively, which, together with the hydrographical properties, demonstrated that the core originated from the AZ (35). Chl *a* within the core was patchy, ranging between 0.7 and 1.2 mg·m$^{-3}$, which is twofold to five-fold higher than average AZ concentrations (37). Phytoplankton carbon (PPC) was dominated by large, spiny, heavily silicified (thick-shelled) diatoms typical of the AZ with nano-flagellate species contributing <30%. Heterotrophic biomass exceeded that of autotrophs and comprised bacteria (26%), protozooplankton (22%), and metazooplankton dominated by copepods (52%), including all larval stages (Fig. 1 *B* and *C*). The initial small salp population declined during the experiment to negligible biomass (38). $^{15}$N and $^{13}$C isotope ratios of suspended organic particles indicated that community biomass was primarily based on recycled nitrogen (39).

**Trends outside the patch.** Outside the patch, dissolved inorganic carbon (corrected for air–sea exchange), nitrate, and phosphate declined by 1, 0.4, and 0.04 mmol·m$^{-3}$, respectively (35), but silicate decreased considerably by 8 mmol·m$^{-3}$ over 5 wk. This decoupling of silicate and nitrate is reflected in the decline of the already low Si* values [Si − nitrate concentrations (4)] from −6 to −14 mmol·m$^{-3}$ (Fig. 2*A*). The decrease of Si* cannot be explained by horizontal mixing inside the eddy (35) and only partly by local patchiness (Fig. S1) and thus is largely due to silicate uptake, which must have been matched by an equally high sedimentation rate, as BSi levels in the mixed layer remained stable at 0.2 mol Si·m$^{-2}$ (Fig. 2*B*). The substantial diatom growth was apparently supported by ammonium reminer-alized from the dissolved organic nitrogen (DON) pool, which declined linearly from ~4 to ~2 mmol N·m$^{-3}$ during the experiment (35). However, after about 3 wk, rising ammonium concentrations (from <0.5 to >0.7 mmol N·m$^{-3}$) suggest that the system switched to net heterotrophy due to iron limitation

of autotrophs [low photochemical efficiency (Fv/Fm ratio) of 0.32] compounded by mounting grazing pressure. This scenario is supported by low autotrophic/heterotrophic biomass ratios between 0.4 and 0.5 (Fig. 1*C*) and by low primary and bacterial production rates (35). Copepods comprised >50% of hetero-trophic biomass, but, although fecal pellet stocks increased sev-enfold during the 5 wk, the contribution of whole pellets and recognizable remnants to vertical flux was minor as the bulk were fragmented in the surface layer and stocks in the subsurface layer were only a small fraction of surface stocks (Fig. S2). In contrast, the stocks of empty and damaged tintinnid loricae, of similar size to pellet fragments, hence with similar sinking rates, did not differ between layers (Fig. S2), indicating that sinking and not destruction was the major loss term here. We conclude that copepods will have played a key role in maintaining the silica-sinking, nitrogen-recycling ecosystem.

**Trends inside the patch.** Inside the fertilized patch, stocks of Chl *a*, POC, and BSi increased linearly following iron addition due to the growth of various large diatom species whose biomass accoun-ted for 97% of the 100-m depth-integrated Chl *a* increase (76–286 mg Chl *a*·m$^{-2}$) from day −1 to day 21 (Figs. 1 *A* and *B* and 2*B*). The subsequent decline was due to mass mortality and sinking of some diatom species, which was partially compensated by continued accumulation of other species, reflected in the uninterrupted linear decline of Si* until the end of the experi-ment (Fig. 2*A*). Nitrate and DON concentrations declined by 1.6 and 1.8 mmol N·m$^{-3}$, respectively, whereas the corresponding decline in Si was 11 (from 19 to 8) mmol Si·m$^{-3}$ with an uptake ratio of Si/(DON + nitrate) of 3.2 and Si/nitrate of 6.9. This indicates that diatoms were responsible for new production and that the species involved were heavily silicified. Inside the patch, BSi/DC, BSi/POC, and BSi/PON ratios increased from 0.5 to 0.8, 0.2 to 0.5, and 1.3 to 2.7, respectively (Fig. 2 *B* and *C*). Similar ratios were found in iron-limited waters outside the patch (Fig. 2*C*). Assuming a diatom C/N ratio of 5, based on the slope of the linear regression between POC and PON inside the patch, the BSi/DN (diatom nitrogen) ratio increased from 2.5 to 4, implying that several of the dominant diatom species had Si/N ratios well above 4 to compensate for weaker silicification of other domi-nant species. The differential accumulation of BSi in the surface layer was due to a combination of sinking out of less-silicified diatoms and increasing populations of heavily silicified species. Our results support the finding that diatom community composi-tion largely determines community silicification in the Southern Ocean (40). Although silica export did not increase in-patch compared with out-patch, iron-induced export of carbon with the sinking frustules amounted to 0.9 mol (10.8 g) C·m$^{-2}$ during the flux event (35).

The populations of 45 of the 55 diatom taxa recorded during EIFEX increased their abundance inside the patch, indicating that artificial iron fertilization can stimulate growth of a broad range of diatom species. Maximum species-specific accumulation rates of the dominant species ranged between 0.03 and 0.10 d$^{-1}$ (0.04–0.13 d$^{-1}$ corrected for dilution) with highest rates associ-ated with largest size and lowest mortality. The species-specific contribution to bloom biomass also depended on cell size, initial cell abundance (which varied by two orders of magnitude), and timing of the decline phase. As a result, the EIFEX bloom was highly diverse with 21 species contributing >85% of bloom biomass.

The species composition of nondiatom phytoplankton changed over the experiment, but, in contrast to the diatoms, their bio-mass remained more or less constant (Fig. 1*B*), apparently kept in check by grazing pressure of protozooplankton and copepods. The same trends and checks applied to the protozooplankton (Fig. S3), including specialized diatom grazers (e.g., *Proto-peridinium* spp.), which are known to be preferred food of copepods (32). Tintinnid ciliates, despite protection by their lo-ricae, were subject to heavier grazing pressure than diatoms as
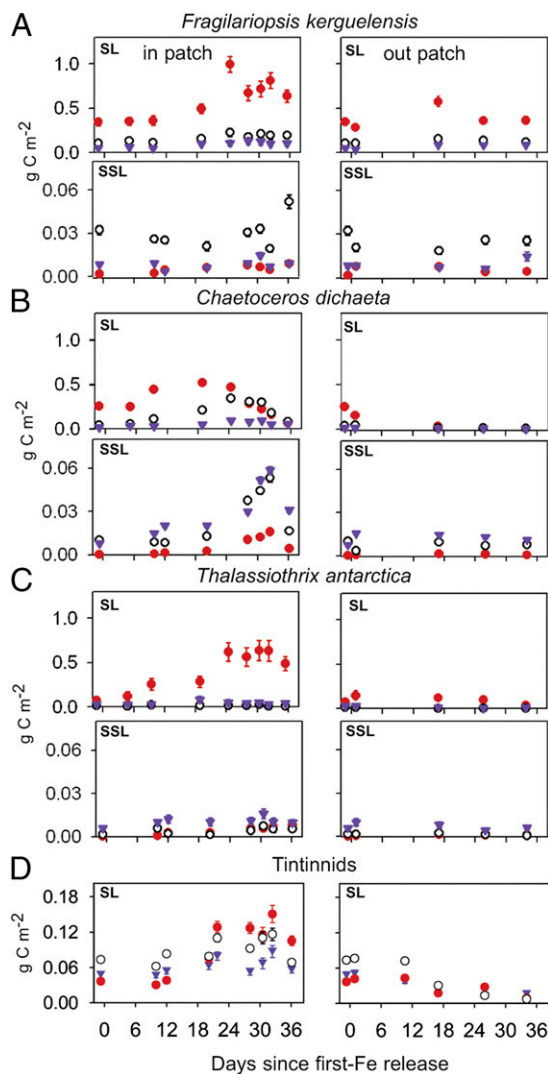
**Fig. 3.** Stocks of three representative diatom species and total tintinnids in surface and subsurface layers. Integrated stocks of full (red filled circles), intact empty (black open circles), and broken diatom frustules and damaged tintinnid loricae (blue triangles) of (*A*) *Fragilariopsis kerguelensis*, (*B*) *Chaetoceros dichaeta*, (*C*) *Thalassiothrix antarctica*, and (*D*) total tintinnids. In each block, the left and right panels are integrated stocks inside and outside the patch, and upper and lower panels are the surface (SL: 0–100 m) and subsurface (SSL: 200–350 m) layers, respectively. Tintinnid stocks are shown for the SL only, and SSL values are in Fig. S2. Full frustules and loricae contain plasma. Empty and broken frustule and loricae numbers are presented as carbon equivalents for comparison with biomass in full frustules and living tintinnids, respectively; bars represent SEs. Note similarity between *F. kerguelensis* stocks inside and outside the patch in SL and SSL, in contrast to the differences in other species. This is supported by a one-sample one-sided *t* test applied to these data (Table S1).

illustrated by the low ratio of full to empty intact and damaged loricae (Fig. 3*D*). The total consumption by microzooplankton (protozooplankton plus small copepods) estimated by the serial dilution method amounted to 17 g C·m$^{-2}$ in 36 d, of which about 30% was provided by bacteria exploiting the DON pool (35). Bacterial biomass was stable but declined at the end of the experiment (Fig. 1*B*). The total bacterial carbon demand over the duration of EIFEX based on measured bacterial production and respiration amounted to 23 g·C m$^{-2}$ of which about one-half was based on prefertilization DON (35), hence independent of primary production.

Biomass of large (>1 mm) copepods increased until the end of the experiment, due to a combination of growth (development of larval stages) and upward migration from below 160 m. Total ingestion by copepods inside the fertilized patch over 36 d, estimated from fecal pellet production rates (Fig. S4*A*), amounted to 20 g C·m$^{-2}$, of which 15 g C·m$^{-2}$ was attributed to phytoplankton carbon indicated by gut evacuation experiments (Fig. S4*B*). Total primary production measured with the $^{14}$C-method amounted to 50 g C·m$^{-2}$ over 36 d (35). Given the large uncertainties associated with all of the above rate measurements, the budget between primary production (50 g C·m$^{-2}$), heterotrophic carbon consumption [~12 g C·m$^{-2}$ (microzooplankton grazing) + 15 g C·m$^{-2}$ (copepod grazing) + ~12 g C·m$^{-2}$ (nitrate-based bacterial carbon demand) ~ 40 g C·m$^{-2}$], and carbon exported (10.8 g C·m$^{-2}$) is reasonably well balanced. Although crushed and intact diatom frustules were prominent in pellets as well as in copepod guts (41), the relative grazing pressure on diatom populations estimated from ratios of full to empty and broken frustules was much lower than on other protists, exemplified here by tintinnid ciliates (Fig. 3*D*). Trends in $^{15}$N and $^{13}$C isotope ratios of suspended particulates indicated that the initial biomass increase was based primarily on nitrate uptake; following the flux event, recycled nitrogen contributed a larger fraction to community biomass (39).

**Silica and Carbon Sinking Species.** The species comprising the diverse assemblage of large diatoms typical of the ACC differed in their impact on magnitude and composition of the vertical flux. This is illustrated by temporal trends in surface and subsurface layers of stocks and relative proportions of full, empty, and broken frustules of three representative species (Fig. 3). These different behavior patterns are of relevance to the silicon paradox. The surface-layer stocks of *Fragilariopsis kerguelensis* doubled inside the patch after 3 wk and maintained the new level for the next 2 wk. Stocks remained more or less constant outside the patch, whereas most other diatom species declined significantly. The contribution of *F. kerguelensis* to total diatom biomass outside the patch rose from 10% to 21% over the 5 wk, implying its superior survival ability under conditions of iron limitation but sufficient silicate and heavy copepod grazing pressure (Fig. 1*C*). In the subsurface layers below and outside the patch, stocks were fairly constant and at similar levels throughout (Fig. 3*A*), implying a steady, downward flux of largely empty chains and solitary frustules. This is consistent with the distribution of *F. kerguelensis* stocks in the deep-water column (Fig. 4*A*), which are threefold higher below 250 m than the deficit between peak and minimum stocks in the surface layer inside and outside the patch. The near constancy of the ratios of empty to broken frustules in the surface layers inside (2.1 ± 0.4) and outside the patch (2.0 ± 0.5), also recorded in a previous experiment (EisenEx) conducted in spring (36), provides further support for controlled, low-level, quasiconstant mortality in this species with sinking out of empty frustules and recycling of cytoplasm in the surface layer (Fig. S5).

The boom-and-bust behavior of a group of disparate species exemplified by *Chaetoceros dichaeta* (Fig. 3*B*) contrasted with the persistent strategy of *Fragilariopsis kerguelensis*. The former species underwent mass mortality in the surface layer, signaled by a sudden increase in empty frustules, followed by a fivefold population decrease due to sinking. The flux event triggered by mass mortality of *C. dichaeta* transported ~10.8 g C·m$^{-2}$ as rapidly sinking aggregates (Fig. S6 *A–C*) into the deep-water column during the last 10 d (35). Sticky, autolyzed cytoplasm, stretched into mucoid sheets along the spines of various species, entangled chains with one another into millimeter-sized aggregates (Fig. S6 *A and B*). The process was accompanied by increased levels of transparent exopolymer particles (Fig. S7) in ambient water. Chains of various species were entrained in the
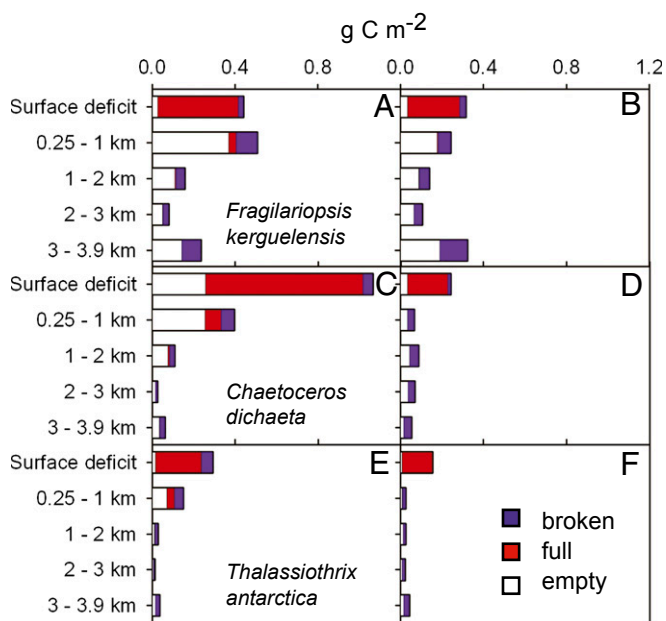
**Fig. 4.** Stocks of three representative diatom species in deep layers in comparison with the surface deficit. Inventories of full (red bars), intact empty (white bars), and broken (blue bars) frustules of (*A* and *B*) *Fragilariopsis kerguelensis*, (*C* and *D*) *Chaetoceros dichaeta*, and (*E* and *F*) *Thalassiothrix antarctica*. The surface deficit was estimated as the difference between peak stocks and the stocks present at the station of the deep profile. Left panels, inside the patch; right panels, outside the patch. The deep in-patch and out-patch profiles were taken on days 36 and 34, respectively, 6–8 d after the flux event commenced. The higher values of *A* and *B* in the deepest layer are partly due to resuspension of sediment in the nepheloid layer. The unexpected low biomass of *C. dichaeta* in deep layers under the patch is due to undersampling by Niskin bottles of large, rapidly sinking aggregates in which they were packed.

aggregates (Fig. S6 *B* and *C*) and mass presence of *Chaetoceros* spp. was only observed under the patch during the flux event, whereas they were at low levels outside it (Figs. 3*B* and 4 *C* and *D* and Fig. S6 *D* and *E*). However, frustule stocks in the deep-water column under the patch were lower than the surface deficit (unlike *F. kerguelensis*) and the bulk was found in the upper 1,000 m (Fig. 4*C*). The depth distribution inferred here from discrete 12-L water samples differed from transmissometer profiles, which recorded a rapid increase in particle stocks in the entire deep-water column during the flux event, albeit with fairly uniform depth distribution (Fig. S8). The discrepancy can be attributed to undersampling by Niskin bottles of large, rapidly sinking aggregates that constituted the bulk of flux below 1,000 m.

The common feature of the remaining, heterogeneous group of largely centric colonial species (in particular *Corethron inerme* and *Proboscia alata*), but exemplified here by the heavily silicified pennate *Thalassiothrix antarctica* (Fig. 3*C*), was the low mortality rate (the ratio of full to empty and broken frustules increased from initially 1.9 to 17.6 by the end of the experiment), which resulted in (*i*) stable or growing populations until the end of the experiment, (*ii*) the highest accumulation rates during the growth phase, and (*iii*) low concentrations in the subsurface and deep layers (Figs. 3*C* and 4 *E* and *F*). The low sinking losses indicate that living cells maintain neutral buoyancy despite massive ballast in the thick cell walls of some species. Because grazing pressure on these species was low, it is likely that a substantial portion of their biomass will have eventually sunk out, indicated by satellite images of fading Chl *a* concentrations in the patch after day 36 (35). Mass sinking events of *T. antarctica* have been reported from the ACC and,

presumably because of its thick cell walls, it is a major constituent of AZ sediments (16, 17).

The behavior of *Fragilariopsis kerguelensis* and *Chaetoceros dichaeta* reflect two distinctly different life cycle strategies characteristic of the pelagic realm: (*i*) maintenance of relatively constant stocks in the surface layer (persistence strategy) and (*ii*) cycles of biomass buildup during favorable growth conditions, followed by mass mortality and rapid population decline (boom-and-bust strategy). These categories represent end points of a gradient along which other ACC diatoms fall. Whereas species of the persistent strategy generally occur at background levels (42), *F. kerguelensis* is a dominant species, which increases in abundance, together with copepod biomass, northward across the AZ (14, 16, 27, 36, 37). This distribution can be explained by its ability to withstand grazing pressure apparently due to its extraordinarily strong frustules (43), which reduces the proportion of cells cracked and crushed by copepod feeding (Fig. S5 *B* and *C*) and facilitates viable gut passage (41, 44). Its increasing abundance across the AZ is concomitant with declining Si* and increasing deposition of its frustules in underlying sediments (Fig. S5*D*; see also refs. 16, 25, and 45). In summary, this species, together with a few others (see below), is a silica sinker responsible for selective silicon export and burial coupled with carbon and nitrogen retention across the surface layer of the iron-limited AZ. Coevolution between diatoms and copepods, which selects for traits at the upper limit of the handling capacity of the herbivores, hence could explain the heavy silicification resulting in high Si/C ratios of open-ocean ACC diatoms (14).

In contrast, species with a boom-and-bust strategy that undergo mass mortality and produce aggregates in the surface layer are carbon sinkers (14, 27, 46) with spiny and needle-shaped species, in particular the genus *Chaetoceros*, most likely to form the large, rapidly sinking aggregates that are responsible for the deepest flux (47). Layers of diatom fluff, widely reported on the seafloor in the aftermath of surface blooms, will be caused by such flux events (48). In the ACC, blooms of boom-and-bust species are local, and characteristic of iron-sufficient waters in the proximity of land masses and in regions of dust deposition (49–51).

Zonally persistent species like *Fragilariopsis kerguelensis* are apparently geared to the copepod-dominated recycling system, which also recycles iron (52). It follows that high sedimentary silica accumulation rates are a proxy for iron-limited diatom assemblages rather than for high surface productivity, contrary to the prevailing view (33, 53). As the bulk of the frustules of carbon-sinking species are not buried (e.g., *Pseudo-nitzschia* and vegetative cells of *Chaetoceros* and *Thalassiosira* except *T. lentiginosa*), they fuel the water column silicon trap, which is partially depleted by burial of exceptionally robust frustules of *F. kerguelensis* and a few other species such as *Thalassiosira lentiginosa*, *Thalassiothrix antarctica*, and *Thalassionema nitzschioides* (16, 25, 45).

During the Last Glacial Maximum (LGM), natural iron fertilization extended the current range of carbon-sinking species from the Antarctic Peninsula across the entire South Atlantic sector of the ACC (54). It is likely that artificial iron fertilization will have a similar effect, i.e., it will extend populations of carbon-sinking species over a larger area that will sink more carbon per silicon than is currently the case. Nevertheless, the upper limit of carbon sequestration will be determined by how much of the upwelling silicate is taken up and exported by carbon-sinking species before exhaustion by silica-sinking species. Given their persistent life cycle strategy geared to the surface recycling system and the silicon-sequestering circulation pattern of the ACC, silica sinkers will always be present in the ACC. Thus, the sedimentary band dominated by *Fragilariopsis kerguelensis* moved north in the LGM (54), implying that its northern boundary will have coincided with the zone of summer surface silicate limitation as is the case today along the APF (18). Indeed, we suggest that such a vertical silicon retention loop, maintained by diatoms and copepods strikingly similar to those of the AZ (14), could

also be responsible for silicon trapping and burial in the HNLC region of the subarctic North Pacific (4).

## Materials and Methods

Water samples were taken with 12-L Niskin bottles mounted on a CTD rosette equipped with a profiling transmissometer and treated according to standard protocols for the various measurements. Prokaryotic abundance was determined by enumerating DAPI-stained cells under the epifluorescence microscope. All eukaryotic organisms were identified as far as possible to the species level and counted by light microscopy. Larger protozoa and copepods <1 mm (including larvae) were concentrated by passing 12 or 24 L through 20-μm mesh gauze. Diatoms and other suspended particles in the deep-water column below 200 m were concentrated over 10-μm mesh gauze. Zooplankton >1 mm were sampled with vertical net tows taken between 0- and 160-m depth to include vertically migrating populations. All organism counts were converted into carbon units using standard protocols. Detailed methods are described in SI Materials and Methods.

1. Falkowski PG, Barber RT, Smetacek V (1998) Biogeochemical controls and feedbacks on ocean primary production. *Science* 281(5374):200–207.
2. Smetacek V (1999) Diatoms and the ocean carbon cycle. *Protist* 150(1):25–32.
3. Dugdale RC, Wilkerson FP (2001) Sources and fates of silicon in the ocean: The role of diatoms in the climate and glacial cycles. *Sci Mar* 65(Suppl 2):141–152.
4. Sarmiento JL, Gruber N, Brzezinski MA, Dunne JP (2004) High-latitude controls of thermocline nutrients and low latitude biological productivity. *Nature* 427(6969):56–60.
5. Pollard R, Treguer P, Read J (2006) Quantifying nutrient supply to the Southern Ocean. *J Geophys Res* 111(C5):C05011.
6. Coale KH, et al. (2004) Southern Ocean iron enrichment experiment: Carbon cycling in high- and low-Si waters. *Science* 304(5669):408–414.
7. Brzezinski MA (1985) The Si-N-C ratio of marine diatoms. Interspecific variability and the effect of some environmental variables. *J Phycol* 21(3):347–357.
8. Sarthou G, Timmermans KR, Blain S, Treguer P (2005) Growth physiology and fate of diatoms in the ocean: A review. *J Sea Res* 53(1-2):25–42.
9. Pondaven P, et al. (2000) Resolving the "opal paradox" in the Southern Ocean. *Nature* 405(6783):168–172.
10. Takeda S (1998) Influence of iron availability on nutrient consumption ratio of diatoms in oceanic waters. *Nature* 393(6687):774–777.
11. Hutchins DA, Bruland KW (1998) Iron-limited diatom growth and Si:N uptake ratios in a coastal upwelling regime. *Nature* 393(6685):561–564.
12. Franck VM, Bruland KW, Hutchins DA, Brzezinski MA (2003) Iron and zinc effects on silicic acid and nitrate uptake kinetics in three high-nutrient, low-chlorophyll (HNLC) regions. *Mar Ecol Prog Ser* 252:15–33.
13. Marchetti A, Cassar N (2009) Diatom elemental and morphological changes in response to iron limitation: A brief review with potential paleoceanographic applications. *Geobiology* 7(4):419–431.
14. Smetacek V, Assmy P, Henjes J (2004) The role of grazing in structuring Southern Ocean pelagic ecosystems and biogeochemical cycles. *Antarct Sci* 16(4):541–558.
15. Hoffmann LJ, Peeken I, Lochte K (2007) Effects of iron on the elemental stoichiometry during EIFEX and in the diatoms *Fragilariopsis kerguelensis* and *Chaetoceros dichaeta*. *Biogeosciences* 4(4):569–579.
16. Zielinski U, Gersonde R (1997) Diatom distribution in Southern Ocean surface sediments (Atlantic sector): Implications for paleoenvironmental reconstructions. *Palaeogeogr Palaeoclimatol Palaeoecol* 129(3-4):213–250.
17. Kemp AES, et al. (2006) Production of giant marine diatoms and their export at oceanic frontal zones: Implications for Si and C flux from stratified oceans. *Global Biogeochem Cycles* 20(4):GB4S04.
18. Cortese G, Gersonde R (2008) Plio/Pleistocene changes in the main biogenic silica carrier in the Southern Ocean, Atlantic Sector. *Mar Geol* 252(3-4):100–110.
19. Tréguer P, et al. (1995) The silica balance in the world ocean: A reestimate. *Science* 268(5209):375–379.
20. DeMaster DJ (2002) The accumulation and cycling of biogenic silica in the Southern Ocean: Revisiting the marine silica budget. *Deep Sea Res Part II Top Stud Oceanogr* 49(16):3155–3167.
21. Blain S, et al. (2007) Effect of natural iron fertilization on carbon sequestration in the Southern Ocean. *Nature* 446(7139):1070–1074.
22. Pollard RT, et al. (2009) Southern Ocean deep-water carbon export enhanced by natural iron fertilization. *Nature* 457(7229):577–580.
23. Cassar N, et al. (2007) The Southern Ocean biological response to aeolian iron deposition. *Science* 317(5841):1067–1070.
24. Seiter K, Hensen C, Schroter E, Zabel M (2004) Organic carbon content in surface sediments—defining regional provinces. *Deep Sea Res Part I Oceanogr Res Pap* 51(12):2001–2026.
25. Crosta X, Pichon J-J, Labracherie M (1997) Distribution of *Chaetoceros* resting spores in modern peri-Antarctic sediments. *Mar Micropaleontol* 29(3-4):283–299.
26. Armand LK, Crosta X, Quéguiner B, Mosseri J, Garcia N (2008) Diatoms preserved in surface sediments of the northeastern Kerguelen Plateau. *Deep Sea Res Part II Top Stud Oceanogr* 55(5-7):677–692.
27. Mosseri J, Quéguiner B, Armand L, Cornet-Barthaux V (2008) Impact of iron on silicon utilization by diatoms in the Southern Ocean: A case study of Si/N cycle decoupling in a naturally iron-enriched area. *Deep Sea Res Part II Top Stud Oceanogr* 55(5-7):801–819.
28. Parsons TR, Lalli CM (1988) Comparative oceanic ecology of the plankton communities of the subarctic Atlantic and Pacific oceans. *Oceanogr Mar Biol Annu Rev* 26:317–359.
29. Pollard RT, Bathmann U, Dubischar C, Read JF, Lucas M (2002) Zooplankton distribution and behaviour in the Southern Ocean from surveys with a towed Optical Plankton Counter. *Deep Sea Res Part II Top Stud Oceanogr* 49(18):3889–3915.
30. Frost BW (1991) The role of grazing in the nutrient-rich areas of the open sea. *Limnol Oceanogr* 36(8):1616–1630.
31. Turner JT (2002) Zooplankton fecal pellets, marine snow and sinking phytoplankton blooms. *Aquat Microb Ecol* 27(1):57–102.
32. Irigoien X, Flynn KJ, Harris RP (2005) Phytoplankton blooms: A "loophole" in microzooplankton grazing impact? *J Plankton Res* 27(2):313–321.
33. Sigman DM, Hain MP, Haug GH (2010) The polar ocean and glacial cycles in atmospheric $CO_2$ concentration. *Nature* 466(7302):47–55.
34. Smetacek V, Naqvi SWA (2008) The next generation of iron fertilization experiments in the Southern Ocean. *Philos Trans A Math Phys Eng Sci* 366(1882):3947–3967.
35. Smetacek V, et al. (2012) Deep carbon export from a Southern Ocean iron-fertilized diatom bloom. *Nature* 487(7407):313–319.
36. Assmy P, Henjes J, Klaas C, Smetacek V (2007) Mechanisms determining species dominance in a phytoplankton bloom induced by the iron fertilization experiment EisenEx in the Southern Ocean. *Deep Sea Res Part I Oceanogr Res Pap* 54(3):340–362.
37. Bathmann UV, Scharek R, Klaas C, Dubischar CD, Smetacek V (1997) Spring development of phytoplankton biomass and composition in major water masses of the Atlantic sector of the Southern Ocean. *Deep Sea Res Part II Top Stud Oceanogr* 44(1-2):51–67.
38. von Harbou L (2009) Trophodynamics of salps in the Atlantic Southern Ocean. PhD thesis (Univ of Bremen, Bremen, Germany). Available at http://nbn-resolving.de/urn: nbn:de:gbv:46-diss000119205. Accessed October 2, 2013.
39. Berg GM, et al. (2011) Variation in particulate C and N isotope composition following iron fertilization in two successive phytoplankton communities in the Southern Ocean. *Global Biogeochem Cycles* 25:Gb3013.
40. Baines SB, Twining BS, Brzezinski MA, Nelson DM, Fisher NS (2010) Causes and biogeochemical implications of regional differences in silicification of marine diatoms. *Glob Biogeochem Cycles* 24:GB4031.
41. Kruse S, Jansen S, Krägefsky S, Bathmann U (2009) Gut content analyses of three dominant Antarctic copepod species during an induced phytoplankton bloom EIFEX (European iron fertilization experiment). *Mar Ecol (Berl)* 30(3):301–312.
42. Yooseph S, et al. (2010) Genomic and functional adaptation in surface ocean planktonic prokaryotes. *Nature* 468(7320):60–66.
43. Hamm CE, et al. (2003) Architecture and material properties of diatom shells provide effective mechanical protection. *Nature* 421(6925):841–843.
44. Hamm C, Smetacek V (2007) Armor: Why, when and how. *Evolution of Primary Producers in the Sea*, eds Falkowski PG, Knoll AH (Elsevier Academic, Burlington, MA), pp 311–332.
45. Esper O, Gersonde R, Kadagies N (2010) Diatom distribution in southeastern Pacific surface sediments and their relationship to modern environmental variables. *Palaeogeogr Palaeocl* 287(1-4):1–27.
46. Green SE, Sambrotto RN (2006) Plankton community structure and export of C, N, P and Si in the Antarctic Circumpolar Current. *Deep Sea Res Part II Top Stud Oceanogr* 53(5-7):620–643.
47. Riebesell U, Wolf-Gladrow DA (1992) The relationship between physical aggregation of phytoplankton and particle flux: A numerical model. *Deep Sea Res* 39(7-8):1085–1102.
48. Beaulieu SE (2002) Accumulation and fate of phytodetritus on the sea floor. *Oceanography and Marine Biology: An Annual Review*, eds Gibson RN, Barnes M, Atkinson RJ (Taylor & Francis, London), pp 171–232.
49. Armand LK, Cornet-Barthaux V, Mosseri J, Quéguiner B (2008) Late summer diatom biomass and community structure on and around the naturally iron-fertilised Kerguelen Plateau in the Southern Ocean. *Deep Sea Res Part II Top Stud Oceanogr* 55(5-7):653–676.
50. Poulton AJ, et al. (2007) Phytoplankton community composition around the Crozet Plateau, with emphasis on diatoms and *Phaeocystis*. *Deep Sea Res Part II Top Stud Oceanogr* 54(18-20):2085–2105.
51. Salter I, et al. (2012) Diatom resting spore ecology drives enhanced carbon export from a naturally iron-fertilized bloom in the Southern Ocean. *Global Biogeochem Cycles* 26:GB1014.
52. Boyd PW, Ellwood MJ (2010) The biogeochemical cycle of iron in the ocean. *Nat Geosci* 3(10):675–682.
53. Anderson RF, et al. (2009) Wind-driven upwelling in the Southern Ocean and the deglacial rise in atmospheric $CO_2$. *Science* 323(5920):1443–1448.
54. Abelmann A, Gersonde R, Cortese G, Kuhn G, Smetacek V (2006) Extensive phytoplankton blooms in the Atlantic sector of the glacial Southern Ocean. *Paleoceanography* 21(1):PA1013.

# Supporting Information

## Assmy et al. 10.1073/pnas.1309345110

### SI Materials and Methods

**Site Selection, Fertilization, and Tracking of the Fertilized Patch.** The eddy was located, and its position during the experiment monitored, in satellite images of sea-surface height (http://argo.colorado.edu/~realtime/gsfc_global-real-time_ssh/). The patch was fertilized by releasing $7*10^3$ kg of dissolved ferrous sulfate in concentric circles around a drifting buoy to yield a concentration of 1.5 nmol·L$^{-1}$ on day 0. Two weeks later, another $7*10^3$ kg of FeSO$_4$ was added to the spreading patch equivalent to 0.34 nmol·L$^{-1}$. The movement of the center of the fertilized patch was tracked by a surface buoy drogued at 18- to 26-m depth, equipped with Global Positioning System receivers and radio as well as ARGOS satellite transmitters. The patch was located with the drifting buoy and by continuous, underway measurements of the photochemical efficiency (Fv/Fm). Within a week, the bloom had accumulated sufficient biomass so that additional tracers (chlorophyll and online $f$CO$_2$ concentrations) were used to locate the part of the patch least affected by dilution with outside water, i.e., with the highest chlorophyll and, in the last week, the lowest $f$CO$_2$ concentration. All in-stations were placed inside this "hot spot," and care was taken to locate it with small-scale surveys before sampling and to keep the ship within it during the stations, which generally lasted about 8 h (1). Some in-stations and casts, although within the patch but subsequently shown to have missed the hot spot, have been excluded. The control "out-stations" were taken within the eddy core well away from the patch but (for logistical reasons) in different locations relative to it. The first station (day −1) was sampled 1 d before iron addition and can be considered as representative of initial conditions for both in- and out-patch stations. In-patch stations always sampled the same water mass; casts taken when the ship inadvertently drifted out of the hot spot were discarded. Out-patch stations were located in different water columns relative to the patch but nevertheless provided a coherent picture of processes in unfertilized water. Vertical coherence of the deep-water column with its respective surface layer was demonstrated by the trajectories of four autonomous APEX (Autonomous Profiling Explorer; Webb Research) floats positioned between 200- and 1,000-m depth over a 2-wk period extending beyond the end of the experiment and by different models based on hydrography and altimeter images. Details are presented elsewhere (1).

**Biological Bulk Properties.** Sampling was carried out with Niskin bottles mounted on a CTD rosette equipped with a profiling transmissometer. Particulate organic carbon (POC), nitrogen (PON), biogenic silica (BSi), chlorophyll $a$ (Chl $a$), and primary production were analyzed using standard protocols (1). Inorganic nutrients (silicate, phosphate, nitrate, nitrite, and ammonium) were measured with a Technicon AutoAnalyzer II system using standard methods. Photosynthetic efficiency (Fv/Fm) was measured online with a fast repetition rate fluorometer. Pigment analyses were performed by HPLC according to (2). Colorimetric measurements of transparent exopolymer particles (TEPs) were performed as described by Passow and Alldredge (3). For TEP microscopy, formalin-fixed plankton samples were filtered onto 0.4-µm Nuclepore Track Etch Membranes (Whatman), stained with Alcian blue, and fixed on CytoClear slides (Osmonics) according to Logan et al. (4).

**Plankton Sampling and Quantification.** *Water samples.* For the qualitative and quantitative assessment of the plankton assemblage, duplicate 200-mL water samples were obtained from Niskin bottles from seven discrete depths between 10 and 150 m at the initial station and at eight in- and four out-patch stations. Plankton samples were taken from the same cast together with all core parameters (Chl $a$, nutrients, pCO$_2$, POC, PON, and BSi). One set of samples was preserved with hexamethylenetetramine-buffered formaldehyde solution and one with Lugol's iodine at a final concentration of 2% and 5% (vol/vol), respectively. Fixed samples were stored at 4 °C in the dark until counting back in the home laboratory. Diatoms and other protists with robust cell walls were enumerated in hexamethylenetetramine-buffered formaldehyde-fixed samples, whereas unarmored species (athecate dinoflagellates, aloricate ciliates, and flagellates) were counted in Lugol's iodine solution. Cells were identified and enumerated using inverted light and epifluorescence microscopy (Axiovert 25 and Axiovert 135; Zeiss) as described by Throndsen (5). Subsamples were settled in 50-mL sedimentation chambers (Hydrobios) for 48 h. Each sample was examined until at least 500 cells had been counted. Uncertainties in cell abundance were estimated assuming a random distribution of cells in the counting chambers (6).

To acquire information on species-specific diatom mortality, whole intact empty and recognizable broken frustules were counted in addition to full cells. Only broken diatom frustules of which >50% of the frustule was recognizable were considered. In the case of *Thalassiothrix antarctica*, only broken ends with apical spines, present at only one end, were counted. As the girdle, composed of numerous small scale-like bands, of *Proboscia* and *Rhizosolenia* species rapidly disintegrates upon cell death, only epivalves and hypovalves with signs of damage were considered. Empty and broken frustules were identified to species or genus level and otherwise grouped into size classes. Empty diatom frustules are easy to recognize and identify, and hence provide valuable information on the incidence of cell mortality in species populations (7). Mortality can be due to a broad range of mechanisms such as (*i*) death due to viral, bacterial, or parasitoid infection, (*ii*) ingestion and digestion of cell contents by protozoa (including pallium-feeding dinoflagellates), and metazooplankton such as salps (copepods and euphausiids damage most, but not all, of the ingested diatoms), (*iii*) cell death due to unfavorable environmental conditions such as light deprivation or nutrient limitation, (*iv*) internal regulation of mortality by mechanisms such as cell lysis and/or apoptosis (programmed cell death), and (*v*) gametogenesis in sexual phases when gametes, and later the zygote, abandon the frustule. Broken frustules are due to crustacean (mainly copepods) biting with or without ingestion. Estimates of mortality rates from the ratios of full to empty and broken frustules are dependent on their robustness and size. Thus, the percentage of frustules crushed beyond recognition varies between species and grazer. For instance, robust frustules such as those of *Fragilariopsis kerguelensis* are likely to withstand damage by smaller copepods better than those of *Pseudo-nitzschia*, which again will perform better than those of *Chaetoceros debilis*. The long, thick-walled frustules of *Thalassiothrix antarctica*, even if broken into small pieces, will hardly escape detection. At the other extreme are small, thin-walled diatom species whose frustule remains can no longer be quantified under light microscopy. Therefore, the high ratios of full and empty to broken frustules (~10:1) of large, conspicuous, needle-shaped species, in particular *T. antarctica* and *Proboscia alata*, recorded throughout the experiment are proof that these species are avoided by copepod grazers in surface and subsurface layers.

For prokaryotic abundance, 10–20 mL of water samples were fixed with 3% (vol/vol) formaldehyde (final concentration), stained with DAPI, and filtered onto 0.2-μm, black polycarbonate filters. DAPI-stained cells collected on the filters were enumerated on a Zeiss Axioplan 2 microscope equipped with a 100-W Hg lamp and appropriate filter sets for DAPI. Prokaryotic abundance was converted to prokaryotic carbon biomass using the factor 20 fg C·cell$^{-1}$ (8).

**Concentrated samples.** An extra CTD cast was sampled for the assessment of larger and less abundant protozoa (radiolaria, acantharia, foraminifera, and heliozoa), large *Phaeocystis antarctica* colonies, fecal pellets, as well as copepods <1 mm (including nauplii, copepodites, and adults of small copepod species). The whole content of one to two Niskin bottles (12–24 L) was concentrated to 50 mL by gently pouring the water through a 20-μm mesh net. Samples were taken at 11 depths between 10 and 350 m at the initial station and at seven in- and four out-patch stations. These samples were supersaturated with strontium chloride to prevent the dissolution of the acantharian skeletons (9).

To follow the sinking of the bloom through the deeper layer of the water column, diatoms as well as other microplankton species were enumerated in concentrated samples from 200-, 250-, 300-, and 350-m depth and two deep CTD casts down to the seafloor on day 36 inside and day 34 outside the patch. Sampling depths in the deep casts were chosen according to the number and magnitude of spikes in the transmissometer profile. In case of the deep samples, the content of one Niskin bottle (12 L) was concentrated down to 50 mL by pouring the water gently through a 10-μm mesh net. Special care was taken not to contaminate the deep samples with surface water by thoroughly washing the nets and tubes with fresh water after each sample collection. All concentrated samples were fixed with hexamethylenetetramine-buffered formaldehyde solution at a final concentration of 2% (vol/vol) and stored at 4 °C in the dark.

**Multi-Net samples.** For the qualitative and quantitative estimation of copepods >1 mm, the water column down to 400 m was sampled at five standard depths (25, 50, 100, 160, and 400 m) with a Multi-Net (55- and 100-μm mesh size) on a regular basis inside and outside the fertilized patch during night and day. For later identification and counting, samples were fixed with hexamethylenetetramine-buffered formaldehyde solution at a final concentration of 4% (vol/vol). Several individuals of the most abundant copepods >1 mm from in-patch and out-patch stations were carefully caught with Bongo nets, kept in 0.2-μm filtered seawater for 24 h at 4 °C, and subsequently deep-frozen at −20 and −80 °C for carbon analysis.

**Estimation of Carbon Content, Depth Integrated Stocks, and Accumulation Rates.** In case of phytoplankton and microzooplankton, at least 10–30 randomly chosen individuals of each species were measured and the average cell size was used to calculate the biovolume from equivalent geometrical shapes (10). The biovolume was converted to cellular carbon content through carbon conversion equations recommended by Menden-Deuer and Lessard (11). The biovolume of empty and broken frustules was also calculated and converted into carbon equivalents for a better comparison with full frustule biomass and BSi standing stocks. Tintinnid cell biomass was calculated as for other ciliates. Because of the large size differences in this group, stocks of empty intact and damaged loricae were converted into species-specific biomass equivalents for direct comparison with loricae containing ciliates (full loricae). In case of foraminifera, the biovolume was determined by assuming a spherical shape and using the longest dimension across the calcite test as the diameter (12). Biovolumes of acantharia were calculated assuming a sphere, or a spheroid shape (13). For adult radiolaria, biovolume was measured as the diameter of the spherical central capsule (13). Biovolumes were

converted to biomass using measured carbon/volume ratio estimates (0.08 mg·mm$^{-3}$ for acantharia, 0.089 mg·mm$^{-3}$ for foraminifera, and 0.01 mg·mm$^{-3}$ for radiolaria and heliozoa) according to ref. 13. The carbon content of the *Phaeocystis* colony skin was estimated using the following relationship: nanograms C colony = 213 × (colony volume in cubic millimeters) (14). At least 30 randomly chosen nauplii of each of the three major copepod taxa present in the samples (calanoid, cyclopoid, and harpacticoid species) were measured to determine the average body volume, which was multiplied by 0.08 to obtain the carbon content (15). The carbon content of copepods <1 and >1 mm was directly estimated from C/N analysis (Carlo Erba NA-1500 Analyzer) of picked individuals according to refs. 15 and 16. Fecal pellet volume (FPV) and fecal pellet carbon (FPC) were calculated using recommended geometrical shapes (11) and a carbon conversion factor of 0.07 mg C·mm$^{-3}$ (17), respectively. Fecal pellets were counted in the following categories: complete, broken with one end missing, or highly fragmented.

The data on particle stocks and species populations of each station are presented as biomass (carbon per square meter) derived from trapezoidal depth integration of measurements carried out on six to nine discrete water samples taken from standard depths at 10- to 20-m intervals in the 100-m mixed layer, 50-m intervals in the 200- to 350-m depth layer and larger intervals for the deep-water column down to the seafloor.

Accumulation rates, i.e., the difference between growth and mortality rates, were calculated by estimating the slope of the regression for the log-transformed values of cell concentrations over the time interval in which exponential increase was recorded. Corrections for dilution due to spreading of the patch are described in ref. 1.

**Statistics Applied to Subsurface Layer Data Presented in Fig. 3.** We applied a one-sample, one-sided $t$ test to ascertain whether the differences in sinking behavior of *Chaetoceros dichaeta*, *Fragilariopsis kerguelensis*, and *Thalassiothrix antarctica* between IN and OUT stations for the subsurface layer (SSL) from 200- to 350-m depth are statistically significant (Table S1). We tested the working hypothesis $\Delta c > 0$ ("higher concentrations at IN stations") against the null hypothesis $\Delta c < 0$ ("lower concentrations at IN stations"). We calculated $\Delta c = c_{IN} - c_{OUT}$, where $c_{IN}$ and $c_{OUT}$ are the biomass concentrations (micrograms of carbon per liter) in case of full cells and abundances (frustules per liter) in case of intact empty and broken frustules inside and outside the patch, respectively. By pooling the $\Delta c$ values over the SSL, we obtained a statistical sample with a sample size $n = 4$. Out-patch days 26 and 34 (since first iron addition) were compared with the respective preceding and subsequent in-patch days. All but one null hypotheses could be rejected on the traditional evidence level $\alpha = 0.05$ and on the evidence level $\alpha = 0.1$ for *C. dichaeta* but not for *F. kerguelensis*. Given the small sample size ($n = 4$) and the sampling time differences between in-patch and out-patch stations, one has to expect quite a bit of statistical noise. However, it needs to be noted that the $P$ values for *F. kerguelensis* were almost always higher, particularly in the case of empty and broken frustules, than those for *C. dichaeta* over corresponding time intervals, showing that frustules of *F. kerguelensis* continuously sank out of the surface layer irrespective of the iron status. In contrast, concentrations of full, empty, and broken *C. dichaeta* were much larger under the patch than outside the patch during the peak of the flux event (IN day 32 versus OUT day 34) as illustrated by the very low $P$ values. The scatter in $P$ values for *T. antarctica* are expected given the very low presence of this species in SSL.

**Carbon Ingestion Rates Estimated from Fecal Pellet Production Experiments.** Fecal pellet production was estimated from experiments conducted with four dominant calanoid copepod species

(*Calanus simillimus*, *Rhincalanus gigas*, *Pleuromamma robusta*, and *Calanus propinquus*) and by allometric scaling to estimate fecal pellet production of juvenile stages and the small species *Ctenocalanus citer*. Experiments were conducted at different in- and out-patch stations over the course of the European Iron Fertilization Experiment (EIFEX). Two to four—depending on the size of the species—healthy, adult females were retrieved from Bongo net catches and transferred into three to five parallel 1- or 2-L incubation bottles containing mixed-layer water collected at the station. Bottles were placed on a slowly rotating plankton wheel at in situ temperature and dim light. After 24 h of grazing on the natural plankton community, the content of the bottles was carefully sieved over 30-μm plankton mesh and fixed with hexamine-buffered formaldehyde [4% (vol/vol) final concentration] for later enumeration and size measurements of fecal pellets. Fecal pellet production estimates from the bottle experiments were multiplied by the abundances of the respective species recorded in the upper 160 m, to obtain total daily carbon ingestion in the field. Respiratory needs were added to the fecal pellet production estimates to account for total carbon ingestion. Copepod respiration was assumed to equal 6.5% of the copepod carbon standing stock per day [18].

Because no copepod biomass data were available for out-station 514 (day 17), the standing stocks from out-station 509 (day 11) were used to calculate the respiratory needs. The daily carbon ingestion by copepods increased fivefold from 0.2 to 1 g C·m$^{-2}$·d$^{-1}$, which amounted in total to 20 g C·m$^{-2}$ over the course of EIFEX (15 g C·m$^{-2}$ for fecal pellet production and 5 g C·m$^{-2}$ for respiratory needs, respectively).

### Carbon Ingestion Rates Estimated from Gut Evacuation Experiments.
Gut evacuation experiments were conducted with abundant copepod species collected inside and outside the fertilized patch with a Bongo net during night and day. The Bongo net (100 and 300 μm) was towed vertically from depths between 150 and 20 m to the surface—depending on the time of day—at a maximum speed of 0.3 m·s$^{-1}$. After retrieval of the net, the content of the cod end was immediately transferred into a cooler with 20 L GF/F filtered seawater at in situ temperature. Still on deck, subsamples were retrieved from the diluted catch on a piece of fine mesh for

determination of the initial gut pigment content (G0). The mesh was packed in aluminum foil and shock frozen at −80 °C. For estimating of gut evacuation rate, a time series of subsequent samples was collected typically after 1, 2, 4, 6, 10, 20, and 30 min. Frozen samples were thawed on board and copepods sorted in a cooled Petri dish under a stereomicroscope at dim light. One to 20 individuals for each species were placed in a 20-mL PE centrifuge vial, covered with 5 mL of 90% (vol/vol) aqueous acetone, and left in a refrigerator for extraction of pigments for 24 h. Pigment concentration was measured with a Turner fluorometer before and after acidification. A correction factor for pigment destruction to nonfluorescent components was included by multiplying the concentration of phaeopigments by 1.5. Calculation of the gut clearance coefficient, $k$, and the gut passage time (GPT), was based on the exponential model of ref. 19:

$$k = (\ln(\text{G0}) - \ln(\text{G}(t)))/t$$
$$\text{GPT} = 1/k,$$

where G0 represents the initial gut content (nanograms of pigment per individual), and G($t$), the gut content at a given time $t$. The quotient of $1/k$ represents the GPT in minutes. Daily ingestion (nanograms of pigment per individual per day) is derived from initial gut content G0 and $k$ according to the equation:

$$I = \text{G0} \times k \times 60 \times 12.$$

A grazing period of 12 h was assumed to account for the observed periodicity in the migration and likely feeding behavior of the copepods. Ingestion rates were obtained by multiplying the initial gut content with the respective gut clearance rate that was experimentally determined. Pigment concentrations were converted to phytoplankton carbon (PPC) using a C:Chl $a$ ratio of 30. For estimation of the grazing rates, PPC ingestion was related to copepod carbon weight and expressed as percentage of body carbon ingested per day (daily ration).

Constant daily rations for the different species were based on findings during this (EIFEX) and a previous iron fertilization experiment (20) as well as on additional literature values (21–24).

1. Smetacek V, et al. (2012) Deep carbon export from a Southern Ocean iron-fertilized diatom bloom. *Nature* 487(7407):313–319.
2. Hoffmann L, Peeken I, Lochte K, Assmy P, Veldhuis M (2006) Different reactions of Southern Ocean phytoplankton size classes to iron fertilization. *Limnol Oceanogr* 51(3):1217–1229.
3. Passow U, Alldredge AL (1995) A dye-binding assay for the spectrophotometric measurement of transparent exopolymer particles (TEP). *Limnol Oceanogr* 40(7): 1326–1335.
4. Logan BE, Grossart H-P, Simon M (1994) Direct observation of phytoplankton, TEP, and aggregates on polycarbonate filters using brightfield microscopy. *J Plankton Res* 16(12):1811–1815.
5. Throndsen J (1995) Estimating cell numbers. *Manual on Harmful Marine Microalgae*, eds Hallegraeff GM, Anderson DM, Cembella AD (UNESCO, Paris), pp 63–80.
6. Zar JH (2010) *Biostatistical Analysis* (Prentice Hall International, London), 5th Ed.
7. Assmy P, Henjes J, Klaas C, Smetacek V (2007) Mechanisms determining species dominance in a phytoplankton bloom induced by the iron fertilization experiment EisenEx in the Southern Ocean. *Deep Sea Res Part I Oceanogr Res Pap* 54(3):340–362.
8. Lee S, Fuhrman JA (1987) Relationships between biovolume and biomass of naturally derived marine bacterioplankton. *Appl Environ Microbiol* 53(6):1298–1303.
9. Beers JR, Stewart GL (1970) The preservation of Acantharians in fixed plankton samples. *Limnol Oceanogr* 15(5):825–827.
10. Hillebrand H, Duerselen CD, Kirschtel D, Pollingher U, Zohary T (1999) Biovolume calculation for pelagic and benthic microalgae. *J Phycol* 35(2):403–424.
11. Menden-Deuer S, Lessard EJ (2000) Carbon to volume relationships for dinoflagellates, diatoms and other protist plankton. *Limnol Oceanogr* 45(3):569–579.
12. Bé AWH, et al. (1977) Laboratory and field observations of living planktonic foraminifera. *Micropaleontology* 23(2):155–179.
13. Michaels AF, Caron DA, Swanberg NR, Howse FA, Michaels CM (1995) Planktonic sarcodines (Acantharia, Radiolaria, Foraminifera) in surface waters near Bermuda: Abundance, biomass and vertical flux. *J Plankton Res* 17(1):131–163.
14. Mathot S, et al. (2000) Carbon partitioning within *Phaeocystis antarctica* (Prymnesiophyceae) colonies in the Ross Sea, Antarctica. *J Phycol* 36(6):1049–1056.
15. Postel L, Fock H, Hagen W (2000) Biomass and abundance. *ICES Zooplankton Methodology Manual*, eds Harris RP, Wiebe PH, Lenz J, Skjodal HR, Huntley M (Academic, London), pp 83–191.
16. Meyer B, Atkinson A, Blume B, Bathmann UV (2003) Feeding and energy budgets of larval Antarctic krill *Euphausia superba* in summer. *Mar Ecol Prog Ser* 257:167–177.
17. Riebesell U, Reigstad M, Wassmann P, Noji T, Passow U (1995) On the trophic fate of *Phaeocystis pouchetii* (Hariot): 6. Significance of *Phaeocystis*-derived mucus for vertical flux. *Neth J Sea Res* 33(2):193–203.
18. Dagg MJ, Vidal J, Whitledge TE, Iverson RL, Goering JJ (1982) The feeding, respiration, and excretion of zooplankton in the Bering Sea during a spring bloom. *Deep Sea Res* 29(1):45–63.
19. Dam HG, Peterson WT (1988) The effect of temperature on the gut clearance rate constant of planktonic copepods. *J Exp Mar Biol Ecol* 123(1):1–14.
20. Schultes S (2004) The role of zooplankton grazing in the biogeochemical cycle of silicon in the Southern Ocean. PhD thesis (Univ of Bremen, Bremen, Germany).
21. Mayzaud P, et al. (2002) Carbon intake by zooplankton. Importance and role of zooplankton grazing in the Indian sector of the Southern Ocean. *Deep Sea Res Part II Top Stud Oceanogr* 49(16):3169–3187.
22. Dubischar CD, Bathmann UV (1997) Grazing impact of copepods and salps on phytoplankton in the Atlantic sector of the Southern Ocean. *Deep Sea Res Part II Top Stud Oceanogr* 44(1-2):415–433.
23. Atkinson A, Ward P, Murphy EJ (1996) Diel periodicity of Subantarctic copepods: Relationships between vertical migration, gut fullness and gut evacuation rate. *J Plankton Res* 18(8):1387–1405.
24. Schnack-Schiel SB, Hagen W, Mizdalski E (1991) Seasonal comparison of *Calanoides acutus* and *Calanus propincuus* (copepoda: Calanoida) in the south-eastern Weddel Sea, Antarctica. *Mar Ecol Prog Ser* 70:17–27.
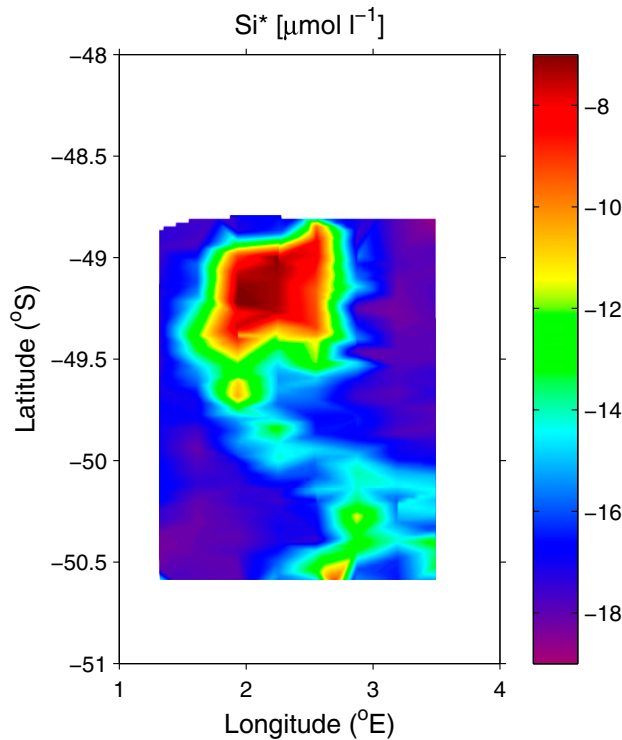
**Fig. S1.** Distribution of Si* during the eddy survey carried out from day 1 to day 7 after fertilization showing clear distinction between the eddy core (the orange/red area) and the surrounding frontal meander.
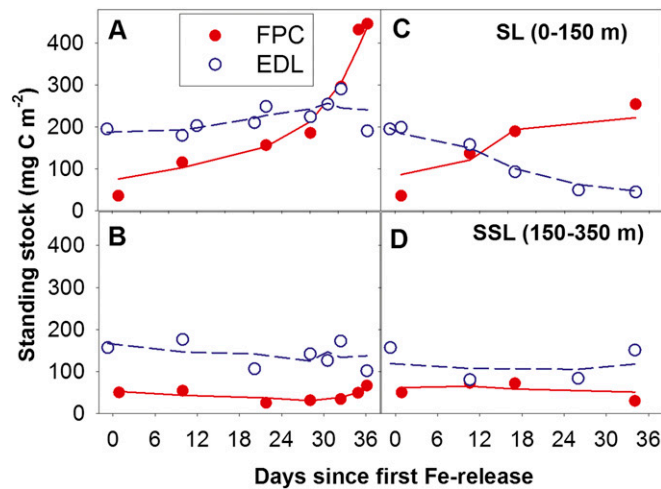


**Fig. S2.** Standing stocks of copepod fecal pellet carbon and carbon equivalents of empty and damaged tintinnid loricae. Copepod fecal pellet carbon (FPC) stocks (the sum of whole pellets and fragments) (filled red circles) and the sum of empty and damaged tintinnid loricae (EDL) presented as equivalent biomass values (open blue circles) integrated for the surface layer (SL: 0–150 m) and the subsurface layer (SSL: 150–350 m) inside (A and B) and outside (C and D) the patch. The lines represent the running average for FPC (solid line) and EDL (dashed line) stocks. Note low pellet stocks in the SSL compared with the surface. We conclude from the difference in stock sizes between SL and SSL and the estimated residence time of pellets in the SL of 24 h that the bulk of pellets produced in the SL was retained there by fragmentation and ingestion. Indeed, generally >80% of all fecal pellets counted were either missing one end or were highly fragmented throughout the upper 550 m of the water column. In contrast, stock sizes of tintinnid loricae, with comparable sinking rates as pellet fragments, are similar in upper and lower layers presumably because of their greater durability. Whole, but often damaged, tintinnid loricae were frequently seen in copepod fecal pellets. Apparently, their leathery consistency (they are also made of proteins) prevent their crushing into small pieces by copepod gnathosomes.
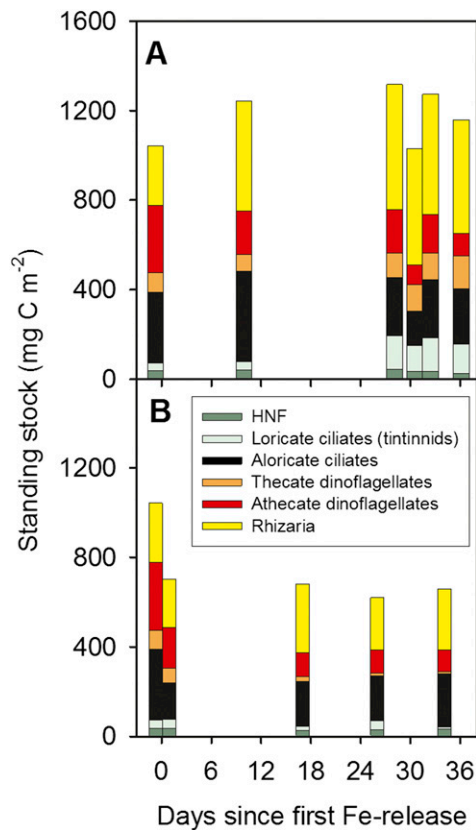
**Fig. S3.** Protozooplankton standing stocks. Protozooplankton standing stocks inside (*A*) and outside (*B*) the patch with contributions of heterotrophic nanoflagellates (HNF), loricate (tintinnid), and aloricate (naked) ciliates (only full loricae were considered in the former), thecate (armored) and athecate (naked) aplastidic dinoflagellates, and Rhizaria (including acantharia, foraminifera, radiolaria, and heliozoa). Note that, despite species succession within each component, their total biomass (with the exception of Rhizaria) did not change significantly during the experiment, which we attribute to heavy grazing pressure exerted by the large copepod community, exemplified by the tintinnids in Fig. 3. Outside the patch, total biomass declined as in the case of all other protistan plankton. Within the Rhizaria, the bulk of the doubling of biomass inside the patch was due to acantharia, a group characterized by numerous outward-pointing, sharp spines made of strontium sulfate. We believe that the large, strong spines provide protection against ingestion by copepods as adult acantharia, although highly conspicuous, were rarely seen in fecal pellets. We conclude that, as in the case of diatoms, low mortality rather than fast growth rates compared with other protists, were the main cause of their increase.
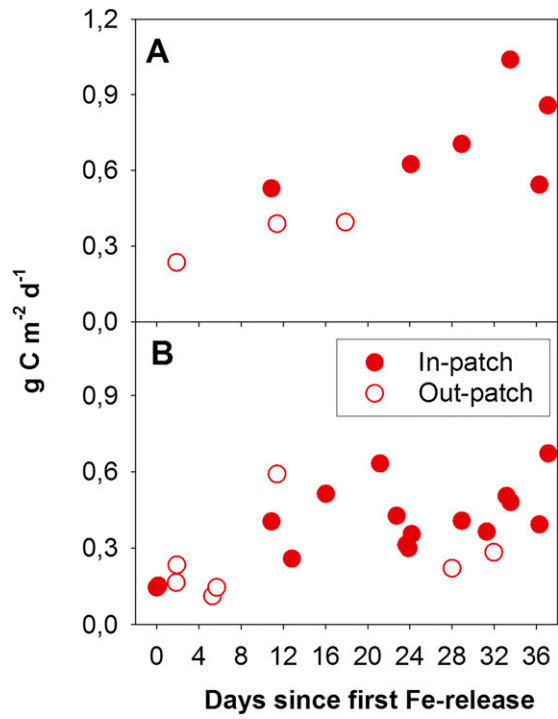
**Fig. S4.** Copepod grazing estimates. (*A*) Total carbon ingestion derived from fecal pellet carbon production experiments, corrected for respiratory needs, of dominant copepod species over the course of EIFEX. (*B*) Phytoplankton carbon (PPC) ingestion rates estimated from copepod gut evacuation experiments over the course of EIFEX. Our grazing estimates are in the same range as those reported from the APF during spring and summer (1, 2).

1. Mayzaud P, et al. (2002) Carbon intake by zooplankton. Importance and role of zooplankton grazing in the Indian sector of the Southern Ocean. *Deep Sea Res Part II Top Stud Oceanogr* 49(16):3169–3187.
2. Urban-Rich J, Dagg M, Peterson J (2001) Copepod grazing on phytoplankton in the Pacific sector of the Antarctic Polar Front. *Deep Sea Res Part II Top Stud Oceanogr* 48(19-20):4223–4246.
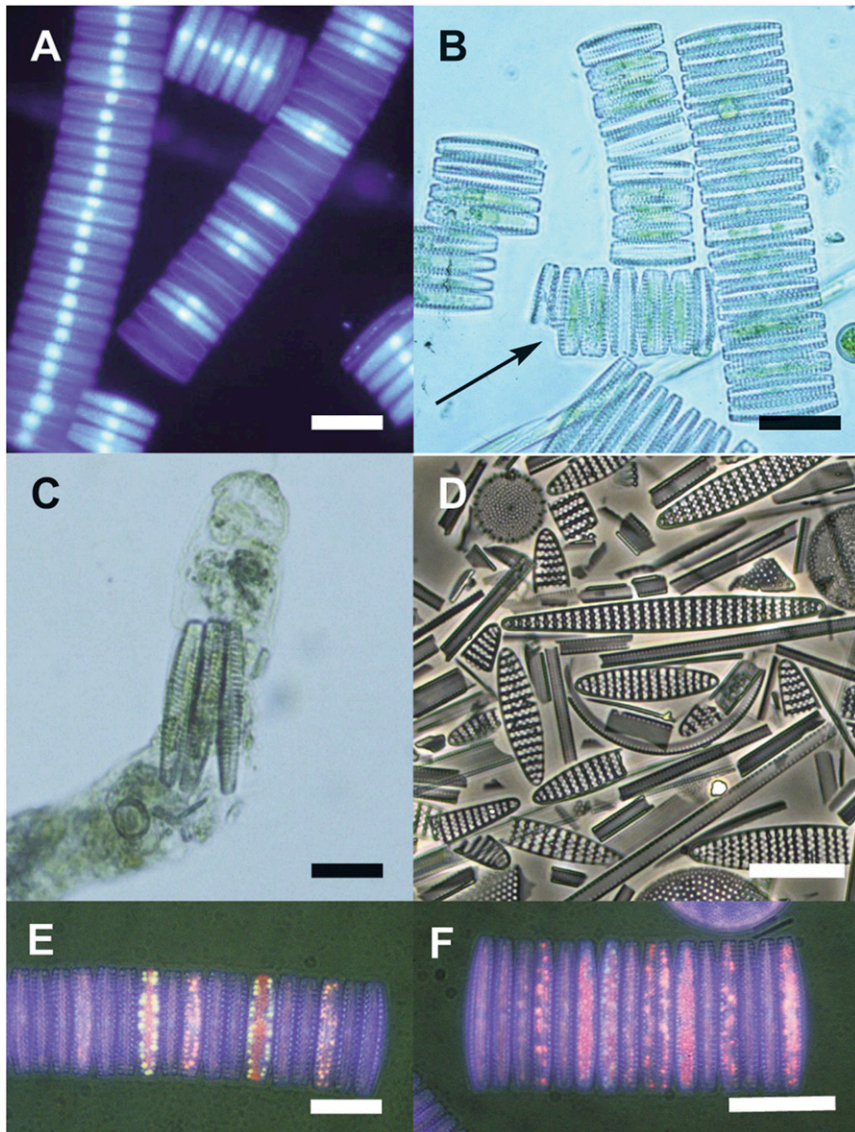
**Fig. S5.** Micrographs of the silica-sinking diatom *Fragilariopsis kerguelensis* collected from field samples. (*A*) Two long chains with nuclei stained with DAPI (a DNA dye) showing numerous empty, intact frustules in one chain. (Scale bar: 50 μm.) (*B*) Intact chains with single bitten terminal cells (marked by arrows) indicate rejection by the copepod after a sampling bout. (Scale bar: 50 μm.) (*C*) Three intact cells inside a copepod fecal pellet. (Scale bar: 30 μm.) Copepods feed sparingly on this species presumably because they are deterred by the energy expenditure and wearing of mandibular teeth associated with crushing the strong frustules, which also increase gut fullness. (*D*) Antarctic sediment sample characteristic of the iron-limited southern Antarctic Circumpolar Current showing dominance of empty, intact valves. (*E* and *F*) Two chains stained with the lipid dye Nile Red showing differentiation of cells within the same chain reflected in large variation in lipid content, implying greater viability in cells with oil droplets. Apoptosis of weaker cells could account for the empty frustules in *A*. Indeed, the cells in a diatom chain are not necessarily identical in terms of viability (1). (Scale bar: 50 μm.)

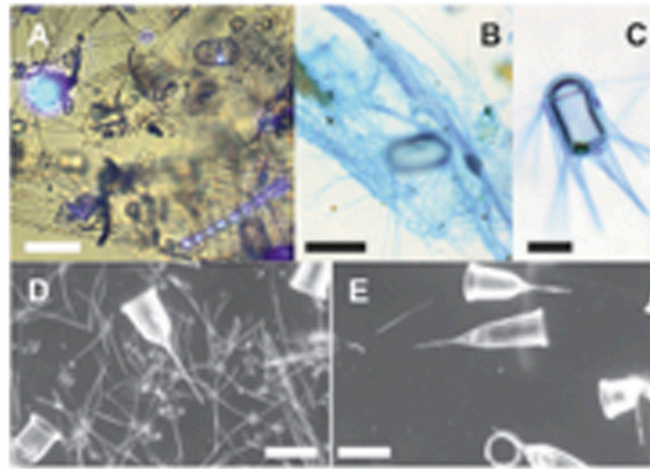1. Laney SR, Olson RJ, Sosik HM (2012) Diatoms favor their younger daughters. *Limnol Oceanogr* 57(5):1572–1578.

**Fig. S6.** Light micrographs of phytoplankton aggregates from 300-m depth under the patch. (*A*) Portion of a 4-mm-long aggregate stained with DAPI (DNA dye) comprising empty and full (with blue nuclei) cells and chains of *Chaetoceros* spp. embedded in a sticky, mucoid matrix. (Scale bar: 100 μm.) (*B*) Empty frustules of *Chaetoceros atlanticus* and *Corethron pennatum* entangled in a mucoid sheath weakly stained by Alcian blue specific for acidic polysaccharides. (Scale bar: 50 μm.) (*C*) Cell of *C. pennatum* oozing out its autolysed, Alcian blue-stained cytoplasm, which has stuck the rigid spines into bundles. (Scale bar: 50 μm.) Multi-Net samples (100-μm mesh) from the layer 160–400 m showing mass presence of *Chaetoceros* spp. under the patch (*D*) during the flux event and absence outside it (*E*). In contrast, empty and damaged tintinnid loricae of *Cymatocylis* spp. are present both underneath the patch and outside it. (Scale bars: 100 μm.)
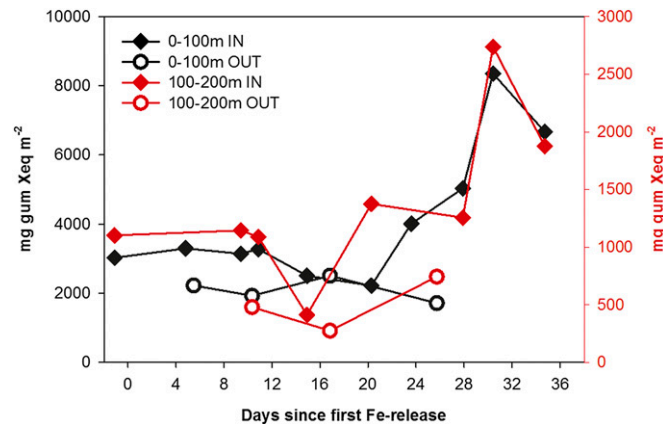


**Fig. S7.** Transparent exopolymer particles (TEPs). Temporal development of TEPs in gum Xanthan equivalents per square meter for the surface layer (0–100 m, black lines and scale) and the subsurface layer (100–200 m, red lines and scale) inside and outside the fertilized patch. Note the strong increase in TEPs during the flux event inside and under the patch.
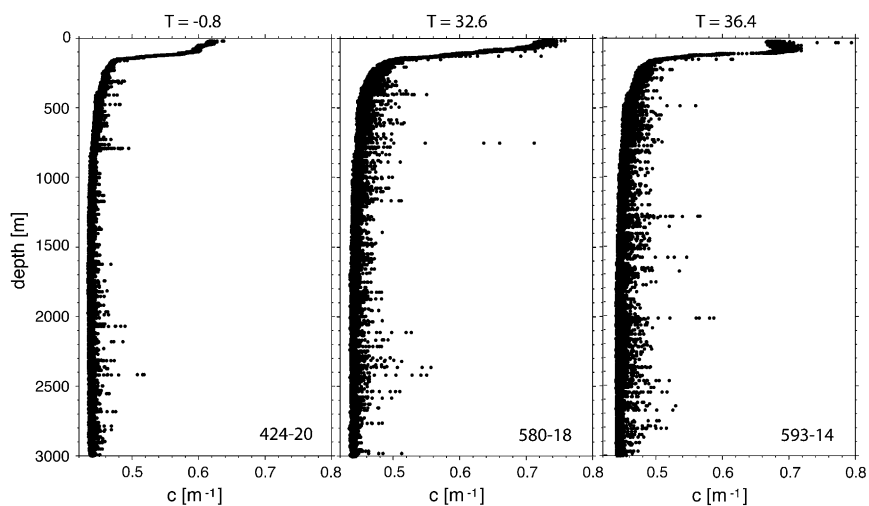
**Fig. S8.** Light beam attenuation profiles for the upper 3,000 m of the water column recorded by the transmissometer under the hot spot before fertilization (day −0.8) and during the flux event on days 32.6 and 36.4. Note the increase in spikes throughout the water column in the end phase of the experiment.

**Table S1. One-sample, one-sided *t* test applied to subsurface layer data presented in Fig. 3**

| Species | IN day | OUT day | P value Full cells | P value Empty frustules | P value Broken frustules |
|---|---|---|---|---|---|
| *C. dichaeta* | 20 | 26 | 0.058 | 0.015 | 0.058 |
| | 28 | 26 | 0.062 | 0.023 | 0.044 |
| | 32 | 34 | 0.0042 | 0.0083 | 0.0019 |
| | 36 | 34 | 0.031 | 0.060 | 0.26 |
| *F. kerguelensis* | 20 | 26 | 0.23 | 0.87 | 0.70 |
| | 28 | 26 | 0.048 | 0.39 | 0.31 |
| | 32 | 34 | 0.23 | 0.92 | 0.94 |
| | 36 | 34 | 0.047 | 0.032 | 0.95 |
| *T. antarctica* | 20 | 26 | 0.037 | 0.67 | 0.096 |
| | 28 | 26 | 0.086 | 0.11 | 0.033 |
| | 32 | 34 | 0.033 | 0.018 | 0.15 |
| | 36 | 34 | 0.098 | 0.020 | 0.44 |

Observed evidence levels (*P* values) for in-patch versus out-patch differences in full cells and empty and broken frustules of *Chaetoceros dichaeta*, *Fragilariopsis kerguelensis*, and *Thalassiothrix antarctica* for the subsurface layer (200–350 m). We have marked *P* values <0.05, <0.1, and >0.1 in red, blue, and black, respectively. For more information, see statistics in *SI Materials and Methods*. Sample size $n = 4$.